PART III

TOXICITY OF ENGINEERED NANOPARTICLES AND RISK ASSESSMENT

15

FATE, BEHAVIOR, AND BIOPHYSICAL MODELING OF NANOPARTICLES IN LIVING SYSTEMS

Emppu Salonen, Feng Ding, and Pu Chun Ke

15.1. INTRODUCTION

In their 2006 commentary, Maynard et al. (2006) highlighted five grand challenges facing nanotechnology: (1) develop instruments to assess exposure to engineered nanomaterials in air and water within the next 3–10 years; (2) develop and validate methods to evaluate the toxicity of engineered nanomaterials within the next 5–15 years; (3) develop models for predicting the potential impact of engineered nanomaterials on the environment and human health within the next 10 years; (4) develop robust systems for evaluating the health and environmental impact of engineered nanomaterials over their entire life within the next 5 years; and (5) develop strategic programs that enable relevant risk-focused research within the next 12 months.

Seven years later, these grand challenges have been partially overcome, judging from the government funding inputs and research outputs in the United States and across Europe and Asia. The rapidly growing literature of physicochemical, medicinal, environmental, and toxicological studies has led to a knowledge base with regard to understanding the fate of nanomaterials in biological systems and at large (Wiesner et al. 2006; Lowry et al. 2012). However, the physical details that are essential for delineating the fundamental aspects of nanomaterial solubility, bioavailability, transformation, transport, and interactions with host systems and, more specifically, the physical methodologies for predicting the potential impact of engineered nanomaterials on the environment and human health have been critically lacking (Ke and Lamm 2011; Gottschalk et al. 2009). This chapter, therefore, serves as an example on how such physical approaches may shed light on our understanding of the fate and behavior of nanoparticles in the aqueous phase and in living systems.

This chapter is arranged as follows. First, we discuss the solubility of carbon-based nanomaterials, namely, carbon nanotubes, fullerenes, graphene, and graphene oxides,

in the presence of natural amphiphiles of gallic acid, natural organic matter, cellulose, fatty acids, and peptides that are building blocks of the biosphere. Second, we show hydrogen bond formation between a fullerene derivative $C_{60}(OH)_{20}$, or "fullerol," and nucleic acids and Taq DNA polymerase; the latter is a machinery responsible for gene amplification *in vitro* and may be regarded as a model system for evaluating the impact of nanoparticles on enzymatic activities *in vivo*. In addition to nucleic acids and DNA polymerase, we investigate the interactions of fullerols with cytoskeletal tubulins as well as with their molecular assembly of microtubules that are essential for cell rigidity, motility, multiplication, as well as cytodieresis—especially for plant cells. More on the biomolecular assembly level, we describe how pristine fullerene and fullerol reach their different energetic minima within a lipid bilayer, and extend results from this study to the interpretations of nanotoxicity for both mammalian and plant cells. Since nanoparticles readily interact with proteins to form a nanoparticle-protein "corona" (Lynch and Dawson 2011), we describe our latest effort on simulating the assembly of ubiquitin—a ubiquitous protein in all eukaryotes—on a silver nanoparticle that is pre-coated with citrate. This study not only allows us to "construct" and "visualize" the formation of protein corona *in silico*, but also demonstrates the remarkable prediction power of computer simulations for illustrating the physical and physicochemical phenomena of protein adsorption and protein-citrate exchange, as well as for deriving the structural information of nanoparticle aggregation and protein crowding that is a precursor for our understanding of nanoparticle-induced immunoreactivity and cytotoxicity.

15.2. SOLUBILITY AND TRANSPORT OF CARBON NANOPARTICLES IN THE AQUEOUS ENVIRONMENT

15.2.1. Measurement of Fullerene Solubility in the Presence of Gallic Acid

Carbon nanostructures, hydrophobic in nature, could gain mobility, bioavailability, and biocompatibility through self-assembly with biomolecules and natural organic matter (NOM) that are abundant in biological and ecosystems (Ke and Qiao 2007). The current lack of understanding involving the specific mechanistic interactions of carbon nanomaterials is both a scientific issue and a deficiency for accurate exposure/risk assessment. Below we show how C_{70}, one class of the most synthesized fullerene species, interact with gallic acids ($C_7H_6O_5$) or GA that are abundant in plant systems (Salonen et al. 2008). The structure of GA is characterized by a carboxyl and three hydroxyls attached to a benzene ring (Figure 15.1); the former functional groups afford the molecule a good solubility and a negative charge at neutral pH, while the latter feature of GA assigns a binding
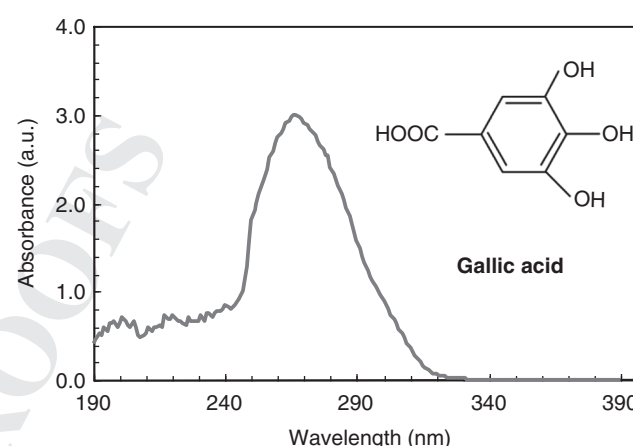

Figure 15.1. (Left) Absorption spectrum of GA (structure see inset). (Right) UV absorbance of C_{70}-GA at a molar ratio of 1:25, recorded at 384 nm. The concentrations of C_{70} in the suspensions were derived from a calibration using dichlorobenzene. *Source*: Salonen et al. 2008. Reproduced with permission from John Wiley & Sons.

mechanism of π-stacking for polyaromatic hydrocarbons as well as fullerenes, graphene, and carbon nanotubes.

C_{70} (MW: 840; Nano-C, Inc.) and GA (MW: 170; Sigma) of molar ratios 1:25 to 1:100 were mixed in Milli-Q water. The mixtures of C_{70}-GA were probe-sonicated (VC 130 PB, Sonics & Materials) at 8 W for 30 min and then placed at room temperature for 3 days. C_{70}-GA suspensions were centrifuged at 6772 RCF for 3 min and then filtered through Microcon (MWCO 3000 Da; Millipore) to remove large clumps of C_{70} particles. The suspensions were further dialyzed for 12 h using DispoDialyzer filters (MWCO 500 Da; Spectrumlabs) to remove free GA. To determine the concentrations of the suspensions, each sample was dried using SpeedVac and the pellets were then dissolved in aromatic solvent 1,2-dichlorobenzene. The quantity of the nanoparticles was then determined using a pre-calibrated absorbance curve for C_{70} in dichlorobenzene (Salonen et al. 2008).

The UV absorbance of C_{70}-GA correlated linearly with the concentration until a plateau was reached at a value of 0.65 mg mL^{-1} (Figure 15.1, right), indicating the limit of C_{70} solubility. Our transmission electron microscopy (TEM) imaging revealed filtered C_{70}-GA complexes as having an average diameter of 20 nm, with each complex encasing multiple C_{70} molecules coated by GA molecules on their surfaces. In addition, "lace-like" clusters ranging from tens of nanometers up to micrometers were observed in the TEM images of the unfiltrated suspensions (Salonen et al. 2008).

15.2.2. Molecular Dynamics Simulation of Fullerene Solvation in the Presence of Gallic Acid

Molecular dynamics (MD) simulations have become a standard tool in soft matter, biophysics, and biochemistry research (Monticelli and Salonen 2012; Berendsen 2007).

This computer simulation technique follows the time evolution of an atomistic or a coarse-grained system by solving the classical equations of motion. While a quantum-mechanical (QM) description of the system of interest would be highly desirable, even with contemporary supercomputer facilities, such an approach is in practice limited to systems comprised of 10^2–10^4 atoms. Moreover, such small systems can only be studied over short timescales which are too brief for describing, for example, supramolecular self-assembly. Instead, a classical approach with the interactions described by a set of physically motivated analytical functions can be used (Monticelli and Salonen 2012; Berendsen 2007; Schlick 2002). The description of the system energy by these empirical potential functions, together with appropriate parameters which have been optimized with respect to experimental and high-level QM data, constitute the *force field* of the system.

The classical/empirical approach is arguably the most widely used computational simulation method in condensed matter physics and chemistry in general. The current state-of-the-art classical force fields (such as CHARMM, GROMOS, OPLS-AA, and AMBER) (Mackerell et al. 1998 and 2004; Oostenbrink et al. 2004; Jorgensen et al., 1988 and 1996; Cornell et al. 1995; Duan et al. 2003) have evolved over the decades to the level of precision where they are not only able to match experimental data well, but also hold *predictive power* for new observations (Monticelli and Salonen 2012; Berendsen 2007; Schlick 2002).

To obtain complementary theoretical insight on the structure and modes of binding of the C_{70}-GA complexes, MD simulations employing the GROMOS 53A6 force field (Oostenbrink et al. 2004) were used to study simple model systems (Salonen et al. 2008). Due to practical reasons, the first model system was limited to a single, small C_{70} cluster in an aqueous environment with GA (anionic), and Na^+ counterions for charge neutrality, simulated over a time of 50 ns. It is experimentally known that an icosahedral cluster (comprised of 13 molecules) of C_{60} is particularly stable in aqueous solution (Andrievsky et al. 2002). We used a similar structure for C_{70}, since the two fullerene species are of similar size and shape and are both hydrophobic. This was indeed observed in our study, where not a single detachment of a C_{70} molecule from the cluster was observed in any of the simulations.

As expected, the GA molecules quickly adsorbed on to the C_{70} cluster surface, within approximately 15–20 ns. The average number of adsorbed GA was 28 ± 2. A similar simulation with only 36 GA resulted in 22 ± 3 adsorbed molecules, indicating that the number of GA enclosing the C_{70} cluster was close to saturation (~2 GA molecules per C_{70} on the cluster surface). Analysis of the orientations of the adsorbed GA showed that practically all the GA aromatic rings were oriented parallel to the adjacent C_{70} surfaces (see Figure 15.2). Such arrangement was driven by maximizing the dispersion interactions between the GA phenyl ring and C_{70} carbon atoms. The adsorbed GA layer was further
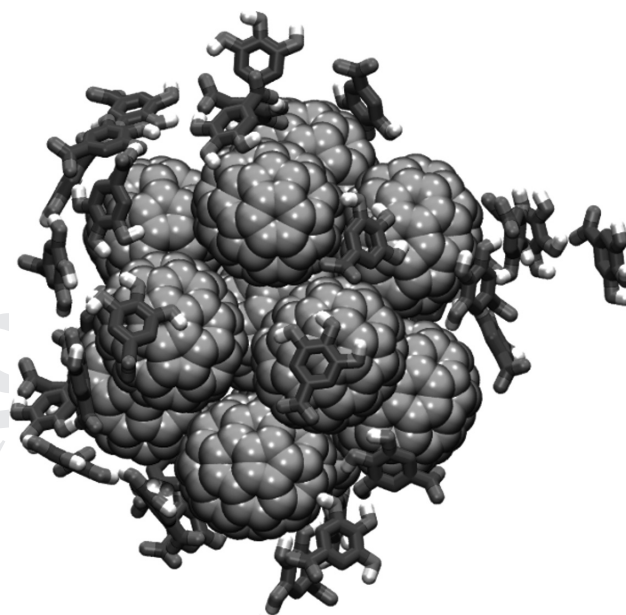

Figure 15.2. An icosahedral cluster of C_{70} (13 molecules in total), with adsorbed phenolic GA molecules. The orientation of the GA phenyl rings parallel to the C_{70} surfaces can be clearly seen. *Source*: Salonen et al. 2008. Reproduced with permission from John Wiley & Sons. The figure graphic was rendered with visual molecular dynamics (VMD) (Humphrey et al. 1996).

stabilized by hydrogen bonding between the GA molecules. It should be noted that the parallel orientation of the GA and C_{70} ring structures was similar to that in π–stacking interactions (Gotovac et al. 2007; Tournus et al. 2005). However, it is possible that in reality the binding of GA to the C_{70} clusters would be stronger than in the MD simulations.

As another model study, the aggregation of single GA-coated C_{70} molecules (with ~5 bound GA molecules per fullerene by average) in aqueous solution was simulated. Again, the bound GA molecules were clearly oriented in such a way that the adjacent GA and C_{70} ring structures were parallel. With 13 such single C_{70}-GA complexes in water with Na^+ counterions, a rapid aggregation was observed. Though the simulation time of 30 ns was clearly insufficient for proper thermodynamic equilibration, it was clear that the C_{70} formed irregular-shaped aggregates, where the binding of adjacent C_{70} molecules was mediated by GA phenyl ring structures. This type of binding was similar to the lace-like structures observed in the TEM measurements (although on a slightly different scale). Such structures also correspond to the suggested mode of binding of polyaromatic hydrocarbons in fullerene aggregates (Yang and Xing 2007).

15.2.3. Measurement of Carbon Nanomaterial Solubility in the Presence of Natural Organic Matter

The binding of carbon nanomaterials with NOM is, mechanistically, similar to the binding of these nanomaterials with

GA due to the comparable physicochemical properties of NOM and GA. The heterogeneous nature of NOM (Hyung et al. 2007; Lin et al. 2009), however, renders another degree of complexity beyond what GA may entail in the binding with nanomaterials.

Naturally occurring Suwannee River NOM (10–100 mg L^{-1}) and tannic acid have both been shown effective in suspending single-walled carbon nanotubes (SWNTs) and multi-walled carbon nanotubes (MWNTs), among which the nanotubes of larger diameters were more stably suspended (Hyung et al. 2007). Humic acid (HA), on the other hand, is a heterogeneous substance and a major constituent of the NOM that may be used as a surrogate for characterizing the behaviors of carbon nanostructures in the natural environment. We first suspended SWNTs (CNI, HiPCO, purity: 75%) and MWNTs (outer diameter: 40–70 nm, 0.5–2 μm in length, purity: 95+%, Aldrich) in the aqueous solution of HA (Fluka, 20% ash, 100 mg L^{-1}). The nominal concentrations of both carbon nanotube suspensions were set at 0.1 mg mL^{-1}, with the weight ratio of the HA to the nanotubes set at 1:10. The mixtures were probe-sonicated for 30 min (VC 130 PB, Sonics & Materials, 8 W) and after settling for over 24 h, the supernatant of each suspension was used for UV-Vis absorbance measurement (Thermo, Biomate 3).

HA alone displayed a yellow color, while MWNTs in HA became a stable suspension. SWNTs, however, precipitated out of water along with HA, yielding the liquid phase colorless (Figure 15.3, left). This result suggests that MWNTs were well dispersed in the HA, while SWNTs formed large bundles prior to their binding to the HA and precipitating out of water. Furthermore, the peak absorbance occurred at 258 nm for the HA and was blue-shifted to 252 nm for MWNT-HA (Figure 15.3, right), indicating π-stacking between the aromatic moieties of the HA and the sp^2-hybridized carbon atoms in the MWNTs.

15.2.4. Molecular Dynamics Simulations of Carbon Nanomaterial Solubility in the Presence of Natural Organic Matter

Following a similar MD simulation approach as in the case of C$_{70}$-GA interaction (see Section 1.2.2), we studied the interaction of CNTs with NOM in aqueous solution. The GROMOS 53A6 force field was chosen, as it has the attractive property of being parameterized, amongst other physicochemical properties, against free energies of solvation of small organic compounds. These small compounds then served as building blocks for larger organic molecules of importance, such as some representative structures of NOM "molecules".

As models for NOM we chose the simple GA and the Temple-Northeastern-Birmingham (TNB) humic acid model structure (Sein et al. 1999). At neutral pH, the TNB model has a charge of –3e, and thus in addition to CNTs and TNB molecules, an appropriate number of Na$^+$ ions was added to make the simulation system charge-neutral. The simulations (Määttä et al. unpublished) featured varying numbers of GA or TNB, interacting with a single (10, 10) SWNT, a bundle of seven SWNTs, as well as an MWNT of comparable size to the bundle.

The anionic GA molecules were observed to rapidly coat the CNT surfaces (see Figure 15.4, left). In the case of a single SWNT, the relative surface coverage of the CNT surface was approximately 0.6. Additional simulations with the neutral form of GA resulted in a surface coverage of up to 0.95 in the case of a single SWNT. As in the case of a C$_{70}$ cluster, the adsorbed GA molecules adopted such orientations that their phenyl rings were parallel to the CNT surfaces.

An efficient surface coverage of the CNTs by the TNB molecules was also seen (Figure 15.4, right). A radial distribution analysis, with respect to the CNT long axes, demonstrated how the aromatic rings of the TNB structure were the closest to the CNT surfaces (as with GA, oriented
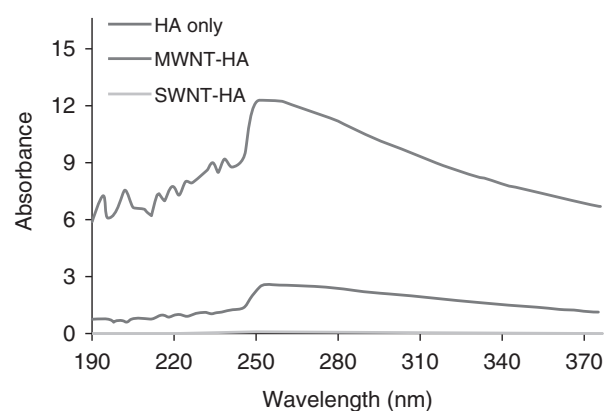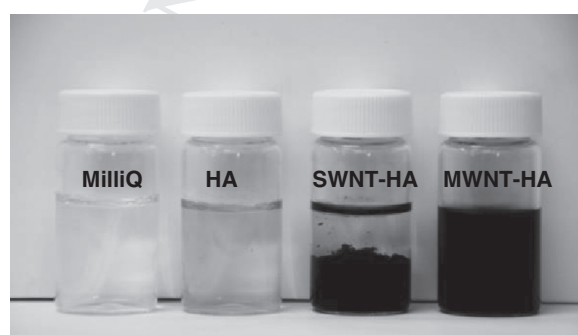

Figure 15.3. (Left) Carbon nanotubes suspended in HA. MWNTs were dispersed in the HA, while SWNTs precipitated out of the suspension together with the HA. (Right) Absorbance of carbon nanotubes in HA. The concentration of HA was 100 mg L^{-1} (pH = 7) for all samples. The nominal concentrations of the MWNTs and SWNTs were 0.1 mg mL^{-1}.
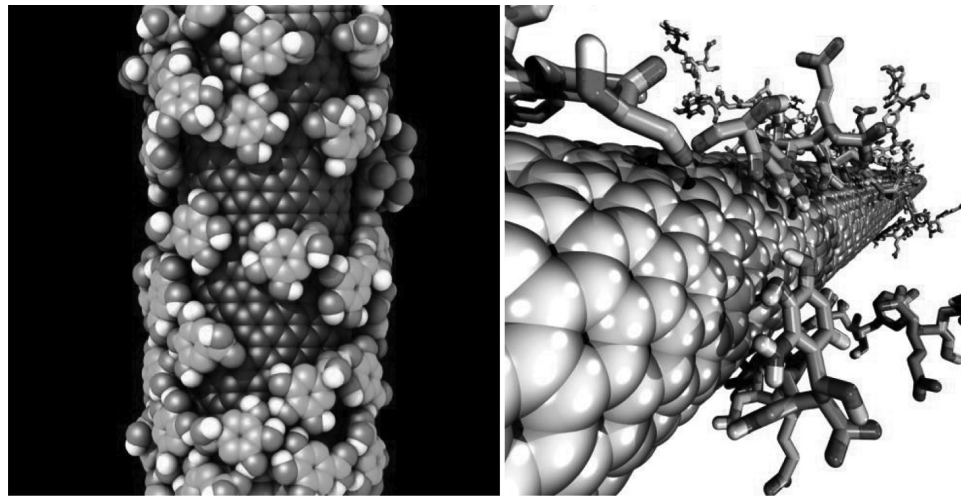
Figure 15.4. GA (left) and the TNB model molecule for NOM (right) adsorbed on SWNT surfaces, as obtained from MD simulations.

parallel to the CNT surfaces), while the hydrophilic carboxyl and hydroxyl groups were oriented towards the aqueous solution. Although further work is needed to, for example, assess the strength of the NOM-CNT binding, these results support the view that NOM is an efficient solubilizing agent for CNTs.

15.2.5. Molecular Dynamics Simulations of Graphene and Graphene Oxide Binding with Natural Amphiphiles

Discharged nanosheets of graphene and graphene derivatives may readily interact with natural amphiphiles that are abundant in the environmental and biological systems. It is the molecular complexes of the graphene derivatives and the natural amphiphiles, that is, their "coronas" (Cedervall et al. 2007), rather than the graphene derivatives themselves that determine the biological and ecological properties of these nanomaterials. Natural amphiphiles are usually comprised of carbohydrates, peptides, and fatty acids. Because of their differences in molecular morphology and physicochemistry, various components of natural amphiphiles may feature distinct binding affinities for the nanosheets. Differences in concentrations and binding affinities of the natural amphiphiles could also lead to competitive binding for the available surfaces of graphene derivatives, similar to the Vroman effect observed for the binding of serum proteins to a substrate (Vroman 1962). Uncovering the molecular mechanism of competitive binding and characterizing the kinetics of corona formation between natural amphiphiles and graphene derivatives will help determine the structure and dynamics of their coronas, which are important for estimating the fate of graphene derivatives in living systems and the natural environment.

Binding of ligands and peptides to graphene derivatives in aqueous solutions has been a subject of interest for both

experimental and computational studies (Sun et al. 2008; Katoch et al. 2012; Pandey et al. 2012). For example, Katoch et al. showed that a dodecamer peptide bound to graphene by orienting its aromatic residues such as tryptophans and histidines parallel to the nanosheet (Katoch et al. 2012). The role of tryptophans for the strong binding of the peptide to graphene was evidenced by comparing the binding affinities of mutant peptides with the tryptophans substituted by alanines. The stability of peptides adsorbed onto a graphene nanosheet was also studied through coarse-grained simulations, which highlighted the importance of π-stacking, van der Waals, and hydrophobic interactions in the binding (Pandey et al. 2012). However, most of these studies were focused on the binding of graphene derivatives with single-molecule and single-component amphiphiles. A systematic study of the binding between graphene derivatives and a collection of representative natural amphiphiles is necessary for elucidating the transformation and transport of graphene derivatives in biological and environmental media.

We applied computational modeling to study the binding of graphene and graphene oxide with natural amphiphiles. In the experiment conducted in parallel, we used algal exudates as a source of the natural amphiphiles. In simulations we adopted cellulose dimer, tri-alanine peptide, and palmitic acid to represent sugar, peptide, and fatty acids in the algal exudates, correspondingly (Figure 15.5). All these three types of biomolecules are found across living species in the ecosystem. We used discrete molecular dynamics (DMD), a rapid sampling algorithm for studying biomolecules (Ding and Dokholyan 2012), to examine the binding *in silico*. The molecule systems were modeled using the united atom representation, where polar hydrogens and heavy atoms were explicitly modeled. The simulations were performed with implicit solvent, and the inter-atomic interactions were modeled by a physical force field adapted from Medusa (Ding and Dokholyan 2006), which included van der Waals, solvation
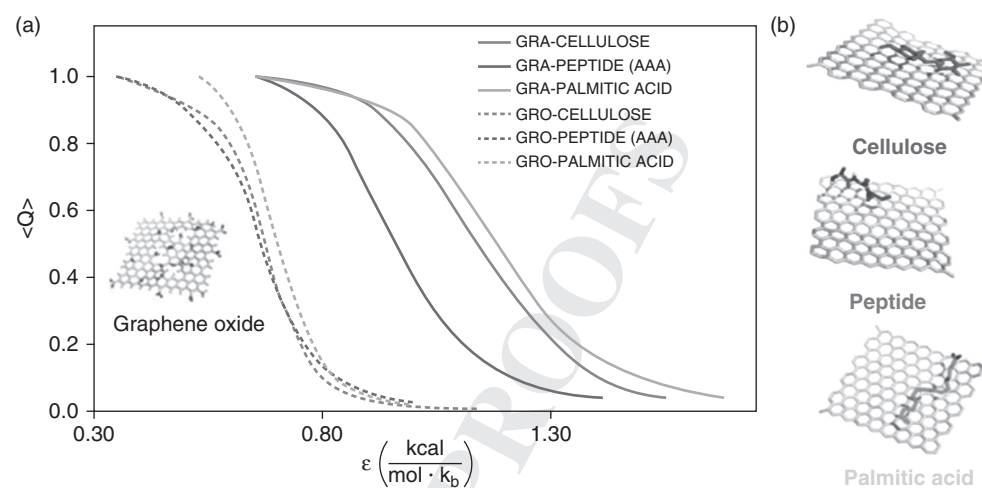
Figure 15.5. Differential binding of graphene (GRA) and graphene oxide (GRO) with natural amphiphiles *in silico*. (a) Fraction (Q) of interaction between natural amphiphile and nanosheet. A Q-value of 1 corresponds to maximum binding. The insert illustrates the model structure of a graphene oxide. (b) Bound conformations between graphene derivatives and natural amphiphiles that include a cellulose, a peptide, and a palmitic acid molecule, respectively. *Source:* Radic et al. 2013. Reproduced with permission from Nature Publishing Group.

(Lazaridis and Karplus 1999), electrostatic, and hydrogen bond potentials. In our simulations, the graphene nanosheet was represented as a two-dimensional honeycomb, where the carbon atoms in the aromatic rings featured van der Waals and hydrophobic interactions. The graphene oxide was modeled by introducing defects, hydroxyl, and carboxyl groups. These modifications rendered the flat surface rugged by altering the carbon hybridization, and the nanosheet became hydrophilic (Figure 15.5).

We found that graphene had a stronger binding to the amphiphiles than graphene oxide (Figure 15.5). The relatively weaker binding of graphene oxide to natural amphiphiles was due to the weaker inter-molecular hydrophobic interactions resulted from various modifications. The observed differences between graphene and graphene oxide were consistent with the experimental characterizations by Raman spectroscopy, scanning electron microscopy, and UV-Vis absorbance spectrophotometry (Radic et al. 2013). For both graphene and graphene oxide, palmitic acid showed the strongest binding while tri-alanine the weakest. The strong binding of palmitic acid to the nanosheet correlated with its long molecular chain consisting of a large number of linear hydrocarbons and high chain flexibility. The conformational flexibility of palmitic acid allowed its long hydrophobic tail to pack against the sheet, highlighting the importance of van der Waals and hydrophobic interactions (Figure 15.5b). Both the cellulose and the peptide were more rigid and more hydrophilic compared to the palmitic acid tail. The higher melting temperature of the cellulose than the peptide on graphene was due to favorable stacking. Contrary to the ring-like structure of cellulose, the peptide backbone of trialanine was not able to form high number of contacts with the nanosheet (Figure 15.5b).

This is in agreement with a previous MD study where lower binding affinity was observed when tryptophan residues were replaced by alanines (Katoch et al. 2012). In the case of graphene oxide, the melting curves of the cellulose and the peptide were close to each other, suggesting the preferable stacking interaction associated with the cellulose was lost as the surface functional groups of the graphene oxide shielded its ring structure.

We also studied the competitive binding of multiple amphiphiles to nanosheet to mimic the interactions of discharged graphene with the biological or environmental milieu. We used the relative ratio of 7:3:1 of glucose to peptide and palmitic acid as found in algal exudates (Haas and Wild 2010), corresponding to 14 cellulose, 6 peptides, and 2 palmitic acid molecules. The amphiphilic molecules were initially positioned away from the nanosheet (Figure 15.6b). We chose the simulation temperature T as the melting temperature for tri-alanine peptide binding. A relatively high temperature allowed rapid equilibration while all molecules could bind to the graphene oxide nanosheet. Due to their high concentrations, the peptides and the cellulose molecules rapidly covered the nanosheet and formed a corona (0-8 ns; Figures 15.6a and 15.6b), which hindered binding of the palmitic acid. However, due to the relatively weak binding affinity, the adsorbed peptides and the cellulose molecules underwent rapid exchanges with the molecules in the solution to form a "soft" corona. Despite its lowest concentration, the palmitic acid molecules occasionally interacted with the dynamic corona through diffusion. Once the nanosheet became available, the palmitic acid molecules bound to the surface and stayed bound during the course of the simulation (Figure 15.6b). In the case of higher stoichiometric ratios of the amphiphiles to the nanosheet, we
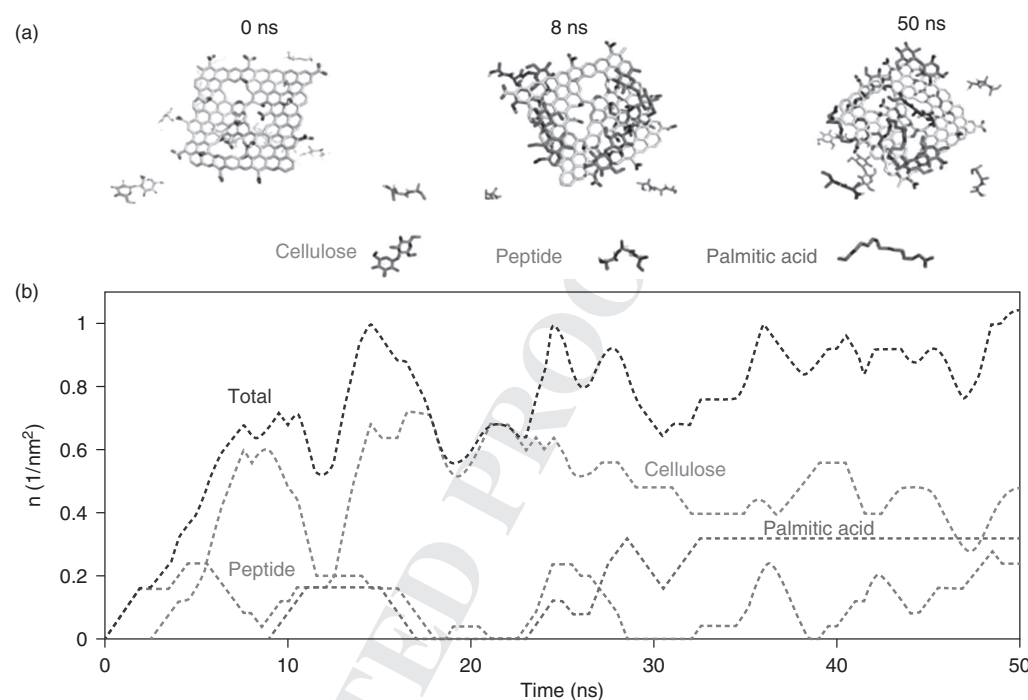
Figure 15.6. Competitive binding of natural amphiphiles with graphene oxide in DMD simulations. (a) Snapshots along the simulation trajectory. (b) Number densities of amphiphilic molecules on the surface of a graphene oxide nanosheet. *Source:* Radic et al. 2013. Reproduced with permission from Nature Publishing Group.

would expect a complete coverage of the nanosheet by strong binders like the palmitic acids to render a "hard" corona. This simulation study of the structure, dynamics, and binding kinetics of graphene derivatives with natural amphiphiles should have great implications for our understanding of the transformation, transport, bioavailability, and toxicity of nanomaterials in biological and ecological systems.

15.3. FULLERENE BINDING WITH NUCLEIC ACIDS

15.3.1. Polymerase Chain Reaction in the Presence of a Fullerene Derivative

While nanoparticles possess realistic chances of entering the environment due to their mobility gained through self assembly with natural amphiphiles such as NOM, GA, and HA, their impact on plants and aquatic organisms is little understood, especially on the molecular level. Among all aspects, the integrity of the genetic material upon its exposure to nanoparticles is perhaps the least studied, despite its apparent biological and toxicological implications. We have recently examined the amplification of a plant heat shock transcription factor (HSTF) gene by real-time polymerase chain reaction (PCR) in the presence of fullerol $C_{60}(OH)_{20}$. This system is simple and artificial, yet it offers opportunities for elucidating the mechanisms of nanoparticles interacting

with nucleic acids and Taq DNA polymerase that are major constituents of the PCR reaction (Shang et al. 2009).

In plants, the HSTF responds to environmental signals such as elevated temperature, regulates developmental and stress-dependent gene regulation, and maintains cellular homeostasis in response to chemical and physiological stresses, oxidative stress, and increased salinity. The PCR primers used in our study were designed based on the genomic DNA sequence of soybean HSTF gene and synthesized by Integrated DNA Technologies, Inc. (IDT, Coralville). The gene was localized within the gene-rich region assigned to the Linkage Group A on the soybean genetic molecular map. Based on our gel electrophoresis assay it became evident that the inhibition of DNA amplification was mainly due to the binding of $C_{60}(OH)_{20}$ with Taq DNA polymerase. The binding of $C_{60}(OH)_{20}$ with free dNTPs, primers, and DNA products also occurred, but did not impact DNA amplification for conventional PCR stoichiometry (Figure 15.7) (Shang et al. 2009).

15.3.2. Molecular Dynamics Simulation of Fullerol Binding with Nucleic Acids

The molecular-scale interactions between fullerol $C_{60}(OH)_{20}$ and dNTPs as well as single-stranded DNA (ssDNA) were investigated by MD simulations (Shang et al. 2009). As in the previous studies, the GROMOS 53A6 force field (Oostenbrink et al. 2004) was used, with the dNTP
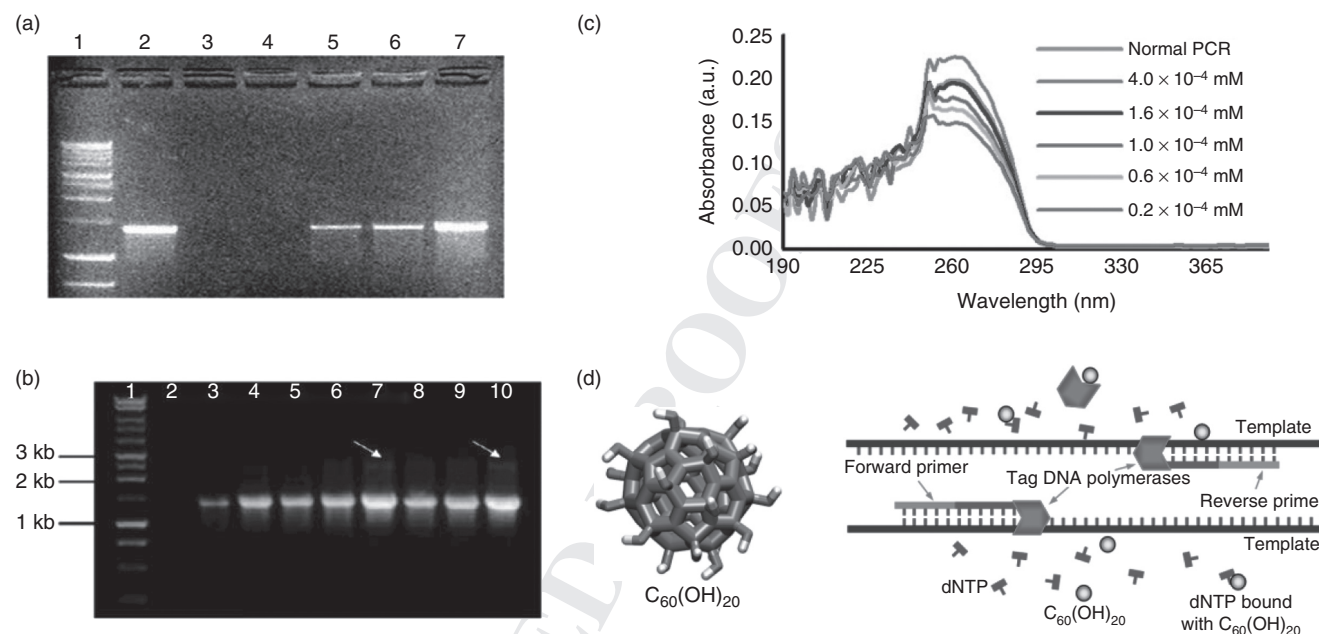
Figure 15.7. (a) PCR products of HSTF amplification. Lane 1:1 kb DNA ladder. Lane 2: normal PCR. Lanes 3–7: PCR with 4.0, 1.6, 1.0, 0.6, and 0.2×10^{-4} mM of $C_{60}(OH)_{20}$, respectively. (b) PCR products of HSTF amplification with additional Taq DNA polymerase. Higher polymerase concentrations yielded stronger amplifications. Lane 1: 1 kb DNA ladder. Lanes 2–4: 4.0×10^{-4} mM of $C_{60}(OH)_{20}$. Lane 2: 1U, Lane 3: 2 U, Lane 4: 4 U. Amplification was detectable for lanes 3 and 4. Lanes 5–7: 1.0×10^{-4} mM $C_{60}(OH)_{20}$. Lane 5: 1 U, Lane 6: 2 U, Lane 7: 4 U. Lanes 8–10: controls. Lane 8: 1 U, Lane 9: 2 U, Lane 10: 4 U. The arrows in (b) indicate spurious amplification products. (c) UV absorbance of real-time PCR products in the presence of different $C_{60}(OH)_{20}$ concentrations. (d) Hypothesized scheme of the interaction mechanism for the PCR-fullerol system. *Source:* Shang et al. 2009. Reproduced with permission from IOP.

parameters adapted from the original parameterization of ATP in the force field. In all cases the systems were made charge-neutral by adding the appropriate number of Na^+ counterions into the model system.

In the case of fullerol-dNTP interactions, the model system focused on the binding of fullerol to a single dNTP (dATP, dTTP, dGTP, or dCTP). The intermolecular binding was studied at two different temperatures, 298 K and 345 K, in order to assess the role of varying temperatures in PCR on the binding process. No qualitative differences in the binding were seen between the two temperatures, indicating that the results of the modeling were representative for the entire PCR cycle. For each choice of dNTP, three independent simulations were carried out. In each case, the dNTP-fullerol pair was simulated over a time of at least 20 ns in a small enough simulation box (side length ∼3.7–3.8 nm) for sufficient sampling of the binding conformations. The general trend for all the dNTPs was very clear: the polyhydroxylated fullerol was predominantly bound to the dNTP triphosphate tail through hydrogen bonding, with an average 4–5 dNTP-fullerol hydrogen bonds in each of the independent simulations. Only negligible amounts of hydrogen bonds between the fullerol and the sugar or base moieties of the dNTPs were observed.

The dNTP-fullerol binding strength was subsequently quantified by radial potential of mean force calculations (that is, the free energy of interaction as a function of the radial center-of-mass distance). In these calculations, which are computationally much more demanding than simple equilibrium simulations, dATP and dCTP were chosen as representative cases. The resulting free energies of binding were 11 ± 3 kJ mol^{-1} and 14 ± 4 kJ mol^{-1} for dATP and dCTP, respectively.

The interaction of ssDNA with a single fullerol molecule was studied. As a simple model for ssDNA, a 20-nucleotide oligomer (5'-CGAAACGAGGGTATCGCGCG-3') was used. Initially, the structure of the ssDNA was set to correspond to the canonical B form in an aqueous solution. After an equilibration of the ssDNA structure over a time of 5 ns, the ssDNA-fullerol interaction was simulated over a time of 40 ns. The conformation and stability of the ssDNA oligomer was monitored by calculating the relative root-mean-square deviation (RMSD) of the constituent atom positions with respect to the initial structure. The simulations showed steady fluctuations around ∼0.75 nm and ∼0.9 nm with and without the fullerol, respectively.

The fullerol was preferentially bound to the ssDNA backbone phosphate oxygens via hydrogen bonding. This was

shown both by calculating the radial distribution functions between the fullerol and different molecular moieties of the oligonucleotide (i.e., backbone, deoxyribose, and bases), as well as hydrogen bonding analysis based on the possible donor-hydrogen-acceptor atom triplets. Hydrogen bonding with the deoxyribose or bases of the ssDNA was insignificant. In contrast to pristine C_{60} or C_{70}, which would readily bind to ring structures by π-stacking-like interactions (see Section 1.2.2), steric hindrance from the hydroxyl groups at the fullerol surface prevented such interactions by the fullerol.

15.4. MOLECULAR DYNAMICS SIMULATIONS OF DNA POLYMERASE INHIBITION BY FULLERENE DERIVATIVES

As shown in the previous section, the MD simulations provided information on the binding of fullerol to dNTPs and ssDNA. However, according to experimental data (Shang et al. 2009; Meng et al. 2007), the limiting factor in PCR inhibition was the Taq DNA polymerase. In order to provide an atomistic insight on fullerol-polymerase interaction, as well as investigate the possible mechanisms of polymerase inhibition, computer simulations were again used. In addition to fullerol, we also used another water-soluble fullerene derivative, fullerene trimalonic acid (TMA), which is also known to inhibit the PCR via affecting the functioning of Taq DNA polymerase (Meng et al. 2007). However, a large-scale MD equilibrium simulation study of a larger protein and a number of fullerene derivatives would require massive computational resources for adequate sampling. And even in such case, there would be no guarantee that the mechanism of inhibition would manifest itself in the $\sim$100–1000 ns timescale of the simulation. Hence, instead of a straightforward, brute force approach, we chose a more rational plan based on the use of two molecular simulation methods: docking and MD (Nedumpully et al. 2012).

Molecular docking is a method widely used to study protein-ligand interactions (Kitchen et al. 2004; Brooijmans et al. 2003). Instead of providing trajectory of the system studied through iteratively solving the equations of motion, as is done in MD, docking does a static sampling of different protein-ligand conformations. The free energy of binding is estimated from an empirical function, unlike the ones used in MD, though further augmented by terms related to the entropic contribution to the free energy. In our case, upon first identifying potential binding sites of the fullerol on the DNA polymerase with docking, subsequent MD simulations with the fullerene derivatives already placed at each binding site of potential importance were carried out.

The docking calculations were carried out with the AutoDock software (Morris et al. 2009), using its default force field (Huey et al. 2007). We considered both the open (DNA-unbound) and closed (DNA-bound) structures of Taq

DNA polymerase (Kim et al. 1995; Li et al. 1998). The calculations revealed a total of eight predominant fullerene derivative binding sites (three for fullerol, five for TMA), with binding free energies in the range of 6–48 kJ mol^{-1}. The binding free energies were overall larger for the anionic TMA (net charge –6e) than for the polar but charge-neutral fullerol. After further consideration on the potential importance of the docking sites for the polymerase inhibition, four sites were chosen for MD simulation studies. In this case we used the OPLS-AA force field (Jorgensen et al. 1988 and 1996) for the protein and a combination of OPLS-AA and parameters specifically optimized for C_{60} by Girifalco (1992) for the fullerene derivatives. The reason for the former choice was that OPLS-AA is known to preserve the native folded structures of proteins quite well, while GROMOS 53A6 is known to favor β-sheets over other protein secondary structures (with respect to experimental data; Matthes and de Groot 2009). The choice of the new parameters for the fullerene derivatives was motivated by the recent validation of this methodology for simulating fullerenes and their derivatives in combination with the OPLS-AA force field (Monticelli 2012).

The fullerol-polymerase systems were simulated at 298 K and 333 K (again, to study the temperature dependence of the findings in order to relate them to the PCR cycle), with Na$^+$ counterions to charge-neutralize the system. In addition to studying the fullerene derivative binding sites suggested by the docking calculations, some simulations with 10 fullerene derivatives randomly placed around the polymerase were also carried out. For each case, the total MD sampling time was in the range of 150–400 ns.

Aside from a single simulation where a fullerol moved a distance of 1 nm on the Taq DNA polymerase surface, the fullerene derivatives placed at their docking binding sites remained there for the entire duration of the MD simulation. In consideration of the long sampling times, this observation verified that the docking sites used were indeed preferable ones for the fullerene derivatives. Simulations at 333 K did not show any noticeable differences in the binding of the fullerene derivatives, nor in the stability of the polymerase structure.

Interestingly, neither the docking nor the MD simulations indicated that the fullerene derivatives would interact directly with the active site of the Taq DNA polymerase. Instead, as one possible mechanism of inhibition, the simulations suggested that the fullerol could bind on the polymerase in the same region as a bound DNA would, in a competitive fashion. However, no such binding was observed for TMA, and experimental data (Shang et al. 2009; Meng et al. 2007) showed that the main mechanism of inhibition cannot be a competitive one, as increasing the concentration of DNA in the PCR solution, while keeping the amount of other molecules the same, did not lead to any reversal of the inhibition.

An important observation was made in the case of a binding site situated in one of the Taq DNA polymerase

subdomains (the so-called "fingers" subdomain) which take part in the open–closed conformational transition upon DNA binding. In a few simulations with fullerene derivatives set at the binding site suggested by docking, it was seen that the polymerase subdomain and another one (the "thumb" subdomain), crucial for the DNA-binding conformational transition, were bound to each other as a consequence of a large-scale movement. The binding was mediated by a fullerene derivative (either fullerol or TMA) in between the polymerase subdomains, with no significant change in the secondary structure of the protein. This type of a tertiary structure change would indeed prevent the binding of DNA and, subsequently inhibit the Taq DNA polymerase activity. More importantly, the mechanism of inhibition would be a non-competitive/mixed one, in line with the experimental data. Such a tertiary structure change was also observed in some simulations with 10 fullerene derivatives initially placed at random positions around the polymerase.

15.5. FULLERENE DERIVATIVES INTERACTING WITH BIOMOLECULAR ASSEMBLIES: MEMBRANES AND MICROTUBULES

15.5.1. Simulations of Membrane Translocation of Pristine and Hydroxylated Fullerene

Inspired by the study by Sayes et al. (2004), we performed atomistic MD simulations of the translocations of both pristine fullerene C_{60} and fullerol $C_{60}(OH)_{20}$ across a dipalmitoylphosphatidylcholine (DPPC) lipid bilayer (Qiao et al. 2007). On one hand this biophysical study illustrated the correlations between the surface chemistries of nanoparticles and their physical interactions with an amphiphilic lipid bilayer, and on the other hand—despite its great simplicity, this study confirmed the *in vitro* observations made by Sayes et al. (2004) that pristine carbon nanoparticles often exert more cytotoxicity than surface coated ones. Specifically, for the hydrophobic fullerene C_{60}, its partitioning into the lipid bilayer and eventual translocation (Figure 15.8) were shown to further facilitate the formation of nanopores in the bilayer. For fullerol, due to its hydrophilic surface functionalization, the nanoparticle merely became adsorbed onto the membrane surface (Figure 15.9) to reduce the area per lipid molecule of the bilayer through both hydrogen bonding and lipid-fullerol dipole-dipole interactions (Qiao et al. 2007).

It should be noted that Wong-Ekkabut et al. (2008) also simulated the process of fullerene translocation through lipid membranes using a coarse-grained model. In their simulation the partitioning of both fullerenes and fullerene clusters partitioning into a dioleoylphosphatidycholine (DOPC) or DPPC bilayer was energetically favorable. After the penetration, clusters disaggregated inside the bilayer quickly. The penetration of fullerenes induced small distortions in the structure and some increase in membrane fluidity. This simulation also suggested that membrane damage due to such penetration was unlikely to occur (Wong-Ekkabut et al. 2008).
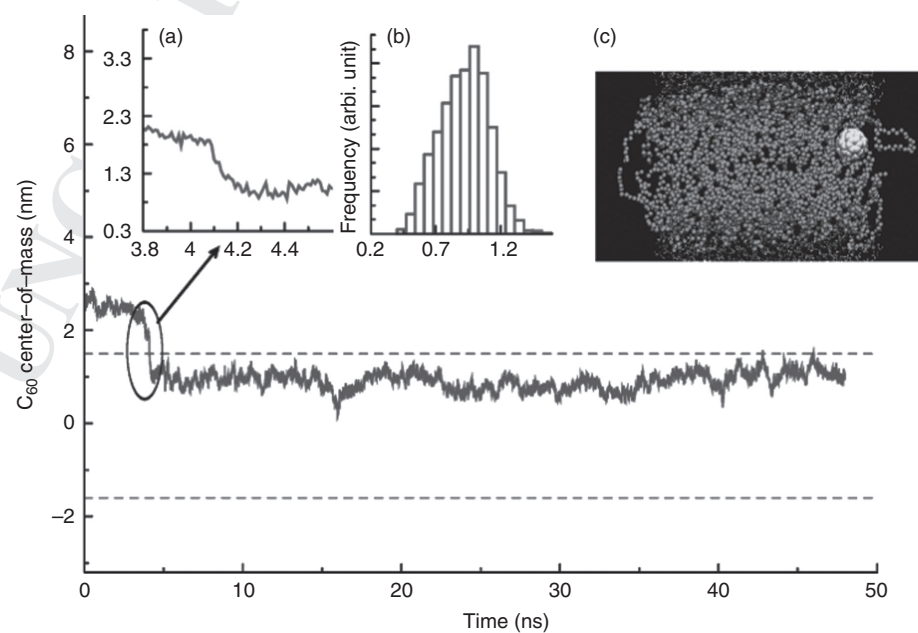

Figure 15.8. Trajectory of C_{60} in the transmembrane (z) direction. The two dashed lines denote the locations of density peaks of the upper and lower leaflet of the DPPC bilayer. (a) Zoomed-in view of the trajectory at $t = 4.09$ ns. (b) Histogram of the z-coordinate of the center-of-mass of the C_{60} molecule after its entry to the bilayer ($t > 4.2$ ns). (c) Side view of the simulation system at $t = 34.5$ ns. The ball denotes the C_{60} molecule, cyan dots denote the lipid tail groups, and the red and blue dots represent the lipid head groups. *Source:* Qiao et al. 2007. Reproduced with permission from American chemical society.
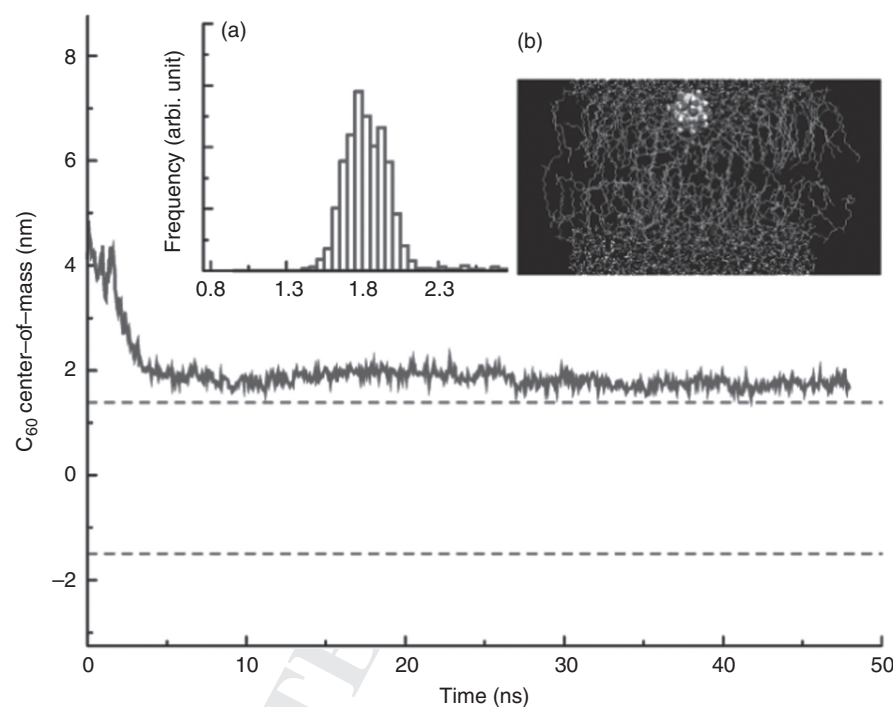
Figure 15.9. Trajectory of $C_{60}(OH)_{20}$ in the transmembrane (z) direction. The two dashed lines denote the location of density peak of the upper and lower leaflets of the DPPC bilayer. (a) Histogram of the z-coordinate of the center-of-mass of $C_{60}(OH)_{20}$ molecule during simulation. (b) Representative side view of the simulation system. The rugged ball denote the $C_{60}(OH)_{20}$ molecule and dots denote the tail and head groups of the DPPC lipids. *Source:* Qiao et al. 2007. Reproduced with permission from American chemical society.

15.5.2. Translocation of Fullerene Derivatives Across a Plant Cell Wall

The aforementioned simulations in Section 1.5.1 clearly showed a direct relevance to our experimental studies of the cytotoxicity of nanoparticles in mammalian systems. Recently we have examined the differential translocation of fullerene C_{70} suspended in NOM (C_{70}-NOM) and fullerol $C_{60}(OH)_{20}$ across the cell walls of plant *Allium cepa* (Chen et al. 2010) and further demonstrated the relevance and prediction power of such simulation work for plant systems.

Figure 15.10 summarizes plant cell damage in the presence of C_{70}-NOM and $C_{60}(OH)_{20}$. Specifically, C_{70}-NOM caused a mere 0.8% more plant cell damage than the control at 90 and 110 mg L^{-1}, and no damage at lower concentrations. This phenomenon is attributed to the large size and hydrophobicity of the C_{70}-NOM, which tended to block the porous plant cell wall through hydrophobic interactions (Figures 15.11b and 15.11c). In contrast, $C_{60}(OH)_{20}$ triggered an increased cell damage with increased concentration (Figure 15.10). The lesser cell damage at 90 and 110 mg L^{-1} is attributed to the gradual aggregation of $C_{60}(OH)_{20}$ at these concentrations, which would have hindered nanoparticle uptake. Due to their small size and good solubility, $C_{60}(OH)_{20}$ readily permeated through the plant cell wall driven by a concentration gradient, and were mostly excluded by the plasma membrane due to their hydrophilicity, mutual electrostatic repulsion, and hydrogen-bonding with water. Under capillary and van der Waals forces these fullerol nanoparticles were confined between the cell wall and the plasma membrane, and accumulate to protrude the plasma membrane driven by their concentration gradient (Figure 15.11e). Since fullerols are relatively inactive in creating reactive oxygen species (ROS), the loss of membrane integrity is inferred as a result of mechanical damage exerted by $C_{60}(OH)_{20}$ aggregation. Such damage would impinge on membrane fluidity, and stress the transport of nutrients and ions between the plant cell and its extracellular space (Chen et al. 2010).

In contrast to our above results where plant cell walls were permeable only to hydrophilic nanoparticles but blocked the translocation of hydrophobic nanoparticles, we observed a completely different scenario for mammalian cells exposed to these two types of nanoparticles. Specifically, the number/density of viable HT-29 mammalian cells decreased with increased C_{70}-NOM concentration up to 70 mg L^{-1}. The cell morphology also changed from the elongated form to the less viable more spherical shapes at higher C_{70}-NOM concentrations, showing abundant nanoparticle aggregates bound to the cell membranes. By comparison, no cell damage was found for HT-29 cells exposed to $C_{60}(OH)_{20}$ of all concentrations, confirming the low affinity of $C_{60}(OH)_{20}$ for
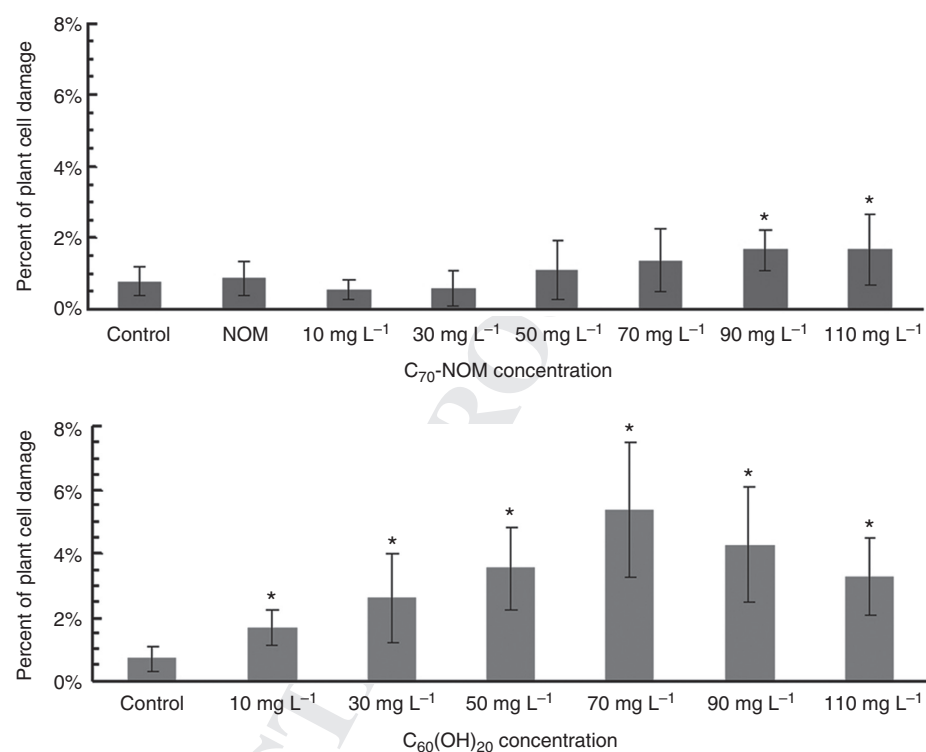
Figure 15.10. Percent of *Allium cepa* plant cell damage in the presence of C_{70}-NOM and $C_{60}(OH)_{20}$ of various concentrations. Incubation time: 9 h. The asterisks indicate data which are statistically different from the control ($p < 0.01$). *Source:* Chen et al. 2010. Reproduced with permission from John Wiley & Sons.

mammalian cell membranes (Chen et al. 2010). These contrasting damages induced by C_{70}-NOM and $C_{60}(OH)_{20}$ to mammalian cells are in good agreement with the *in vitro* study by Sayes et al. (2004) and our simulations (Qiao et al. 2007). This suggests that C_{70}-NOM impacts mammalian cells similarly to C_{60}, possibly due to the hydrophobicity and dissociation of C_{70}-NOM to facilitate C_{70} interacting with the fatty acyl chains in the lipid bilayer.

15.5.3. Molecular Dynamics Simulations on Microtubule Polymerization Inhibited by Fullerol

As in the case of Taq DNA polymerase interacting with fullerene derivatives (cf. Section 1.4), both docking and MD simulations were used to assess the possible binding sites of fullerol $C_{60}(OH)_{20}$ on the tubulin dimer, and to further study how the binding of the fullerol affects the structure and dynamics of tubulin (Ratnikova et al. 2011). The docking calculations were carried out with the AutoDock software (Morris et al. 2009), while the MD simulations used the GROMOS 53A6 force field (Oostenbrink et al. 2004).

The docking simulations revealed 8 important binding sites, with binding free energies in the range of 12–27 kJ mol^{-1}, at both ends of the tubulin dimer, as well as at the interface of the α- and β-tubulins. Interestingly, no binding site was found near the E-site of the dimer.

Two sets of MD simulations were carried out. In the first set, an α-β tubulin dimer was simulated with GTP and GDP bound to it, according to the crystal structure (Lowe et al. 2001). In the second set, 10 fullerol molecules were initially set in random positions around the tubulin dimer with bound GTP and GDP. In addition to these molecules, the model system contained the appropriate number of Na$^+$ counterions, as well as Na$^+$ and Cl$^-$ ions corresponding to a concentration of 100 mM. Four independent simulations, each 50 ns in length, were carried out for both set-ups.

The MD simulations did not show any clear preferential binding site for the fullerols, in agreement with the docking calculations and the stoichiometric analysis of the ITC data. Once the fullerols had reached the tubulin dimer surface, they remained tightly bound to the protein for the remainder of the simulations (see Figure 15.12). As is typical to fullerols with a large number of hydroxyl groups at their surface, the predominant binding interaction with the protein was the formation of hydrogen bonds, on average approximately six per fullerol molecule (Ratnikova et al. 2011).

While no major interaction of the tubulin-bound GTP/ GDP molecules with the fullerols was observed (most likely due to steric hindrances at the GTP/GDP binding sites) (Ratnikova et al. 2011), the MD simulations offered two other plausible mechanisms for the inhibition of the microtubule polymerization. First, fullerols bound at the ends of the
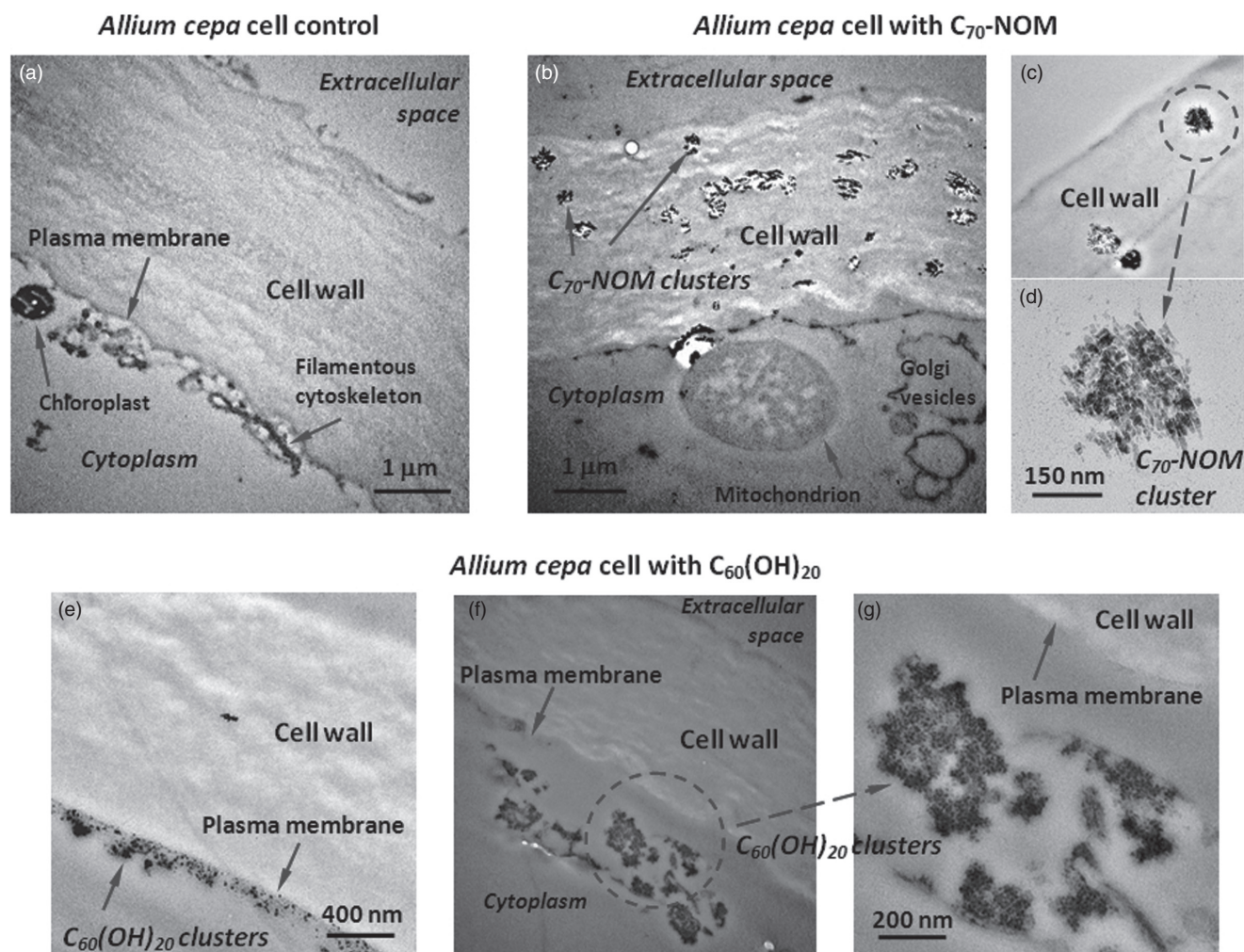
Allium cepa cell control

Allium cepa cell with C$_{70}$-NOM

Allium cepa cell with C$_{60}$(OH)$_{20}$

Figure 15.11. (a) Control showing plant cell wall and plasma membrane. The cell wall typically bends toward its intracellular space. (b–d) Plant cell walls entrapped with C$_{70}$-NOM clusters of 50–400 nm. C$_{70}$-NOM concentration: 50 mg L^{-1}. (d) Magnified view of a C$_{70}$-NOM cluster in (c). (e–g) Translocation of C$_{60}$(OH)$_{20}$ across plant cell walls. C$_{60}$(OH)$_{20}$ clusters can be seen (e) near the interface between the plant cell wall and the plasma membrane and (f, g) in intracellular space. C$_{60}$(OH)$_{20}$ concentration: 50 mg L^{-1}. (g) Magnified view of the C$_{60}$(OH)$_{20}$ clusters in (f). *Source:* Chen et al. 2010. Reproduced with permission from John Wiley & Sons. (*For a color version of this figure, see the color plate section.*)

tubulin dimer could clearly affect its binding with its *longitudinal* neighbors in a protofilament. Indeed, out of the eight important binding sites found in the docking calculations, five would be located at the interface of adjacent dimers in a protofilament. Second, in the *lateral* binding of adjacent tubulin dimers, a major contribution arises from interactions of the so-called M-loop of one dimer with the H5 and H12 helices of another dimer (Lowe et al. 2001). The MD simulations showed that the fullerols have a tendency to bind to all of these locations. The simulations thus suggest that the perturbation of both the longitudinal and lateral binding of tubulin dimers by fullerols contribute to the inhibition of the microtubule polymerization.

15.6. SILVER NANOPARTICLE-UBIQUITIN CORONA

Upon entering biological systems such as the bloodstream, a nanoparticle forms molecular complexes with encountered proteins to render a protein corona (Cedervall et al. 2007). On one hand, the protein corona may shield the surface of the exogenous nanoparticle and subsequently determine the biological properties of the nanoparticle core. On the other hand, interactions with nanoparticles could also alter the structure, dynamics, and function of the bound proteins to further impact recognition of the nanoparticles by membrane receptors and immune systems. Previous experimental
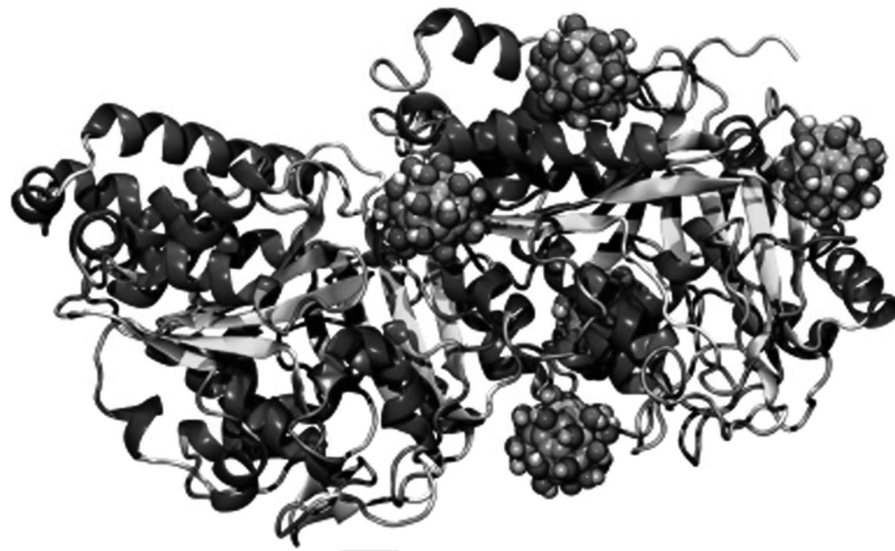
Figure 15.12. MD simulation of fullerols interacting with a tubulin dimer. Water, counterions, and some of the fullerols have been omitted from the figure for clarity. *Source:* Ratnikova et al. 2011. Reproduced with permission from American chemical society.

studies have provided much insight into the existence, size, and composition of the protein corona (Nel et al. 2009). However, the molecular details of protein-nanoparticle interactions remain poorly understood. We have recently performed both computational and experimental characterization of protein corona formation between a silver nanoparticle (AgNP) and ubiquitin. AgNPs are widely used in commercial products for their antibacterial and antifungal properties (Sotiriou and Pratsinis 2010), while ubiquitin is a protein expressed in all eukaryotes regulating protein distribution and recycling, thus making AgNP-ubiquitin a representative model system for studying nanoparticle-protein interactions in mammalian systems and the environment.

Two major challenges arise in computational modeling of protein corona. First is the large system size where an abundance of proteins interacts with nanometer-sized nanoparticles, second is the long timescales associated with protein corona formation. Traditional molecular dynamics approaches can accurately describe nanoparticles and proteins (Ge et al. 2011; Zuo et al. 2010), but are unable to reach the time and length scales relevant for depicting their interactions toward equilibration. To overcome this barrier, we adopted a multiscale modeling approach (Ding and Dokholyan 2005), which coherently blended atomistic and coarse-grained simulations (Ding et al. 2005; Ding et al. 2012). All-atom simulations were first performed to investigate the possible binding modes between an individual ubiquitin and an AgNP, and knowledge of AgNP-ubiquitin binding was then incorporated into the construction of a coarse-grained model. With the coarse-grained simulations, we extensively characterized the structure and dynamics of AgNP interacting with up to 50 ubiquitin molecules. The

dynamics of both atomistic and coarse-grained models were sampled by DMD (Rapapport 1997).

To evaluate whether ubiquitins could bind to an AgNP, we performed DMD simulations near room temperature with a ubiquitin initially positioned away from a citrate-coated AgNP (Figure 15.13a). Interestingly, we found that the neutrally charged ubiquitin did not bind to the hydrophobic surface of the AgNP, but instead was attracted to the surface charge of the AgNP by replacing its surface-bound citrates ($-3e$ at neutral pH) that were stabilized by electrostatic interactions (Figure 15.13a). Near the surface of the ubiquitin helix, negatively charged residues formed a cluster with low electrostatic potentials (Figure 15.13b), which allowed stronger binding to the AgNP than the negatively charged citrates. We also identified the residues important for binding AgNP in simulations. Importantly, one of the AgNP-binding residues, aspartic acid (Asp18), had been experimentally determined to bind gold nanoparticle (AuNP) by nuclear magnetic resonance (NMR) studies (Calzolai et al. 2010). Since AgNP and AuNP are comparable both physically and chemically, we believe that their modes of binding with ubiquitin are also comparable. This agreement between NMR observations and simulations highlights the predictive power of our computational methods.

It is necessary to include multiple proteins to observe the formation of AgNP-ubiquitin corona *in silico*. Such a system, however, is beyond the capacity of atomistic simulations. Instead, we used a two-bead-per-residue model (Ding et al. 2002a) to represent ubiquitin and a single atom to model each citrate. The inter- and intra-ubiquitin interactions were modeled by a structure-based potential model (Ding et al. 2002b; Yang et al. 2004), which has been extensively used in
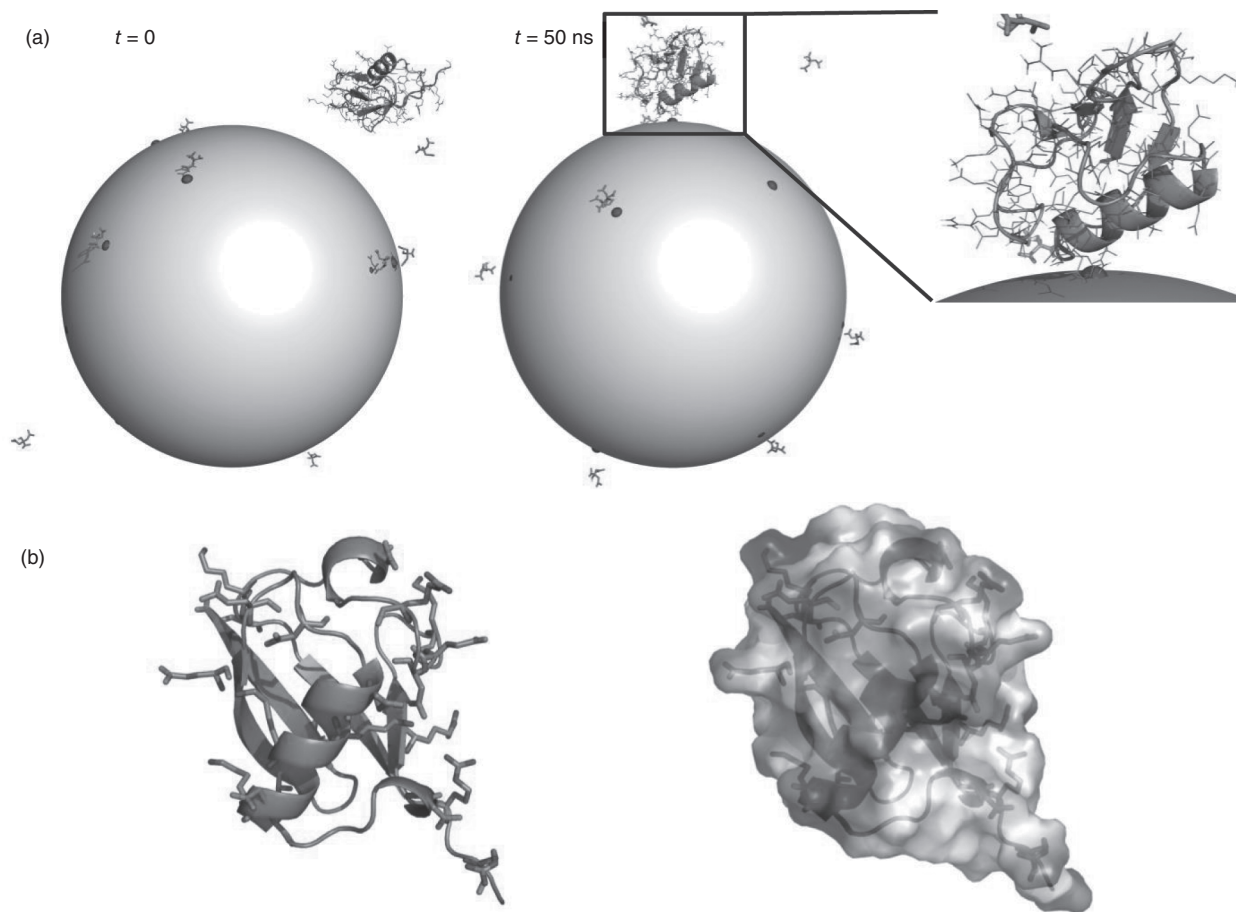
Figure 15.13. Interaction between a single ubiquitin and a citrate-coated AgNP. (a) Initial ($t = 0$ ns) and final ($t = 50$ ns) structure of the ubiquitin-citrate-AgNP complex. The ubiquitin is represented as a cartoon, its side chains as lines, and the citrates as sticks. The gray sphere represents the nanoparticle, and the charged atoms on the AgNP surface are shown as blue spheres. Zoom-in view of the final structure indicates binding between the ubiquitin and a charged AgNP surface atom. (b) The positively and negatively charged residues in ubiquitin are shown as sticks (left panel). The surface electrostatic potential (computed using PyMol, www.pymol.org) illustrates the cluster of negatively charged atoms near the protein helix (right panel). *Source:* Ding et al. 2013. Reproduced with permission of Royal Society of Chemistry. (*For a color version of this figure, see the color plate section.*)

computational studies of protein folding and protein aggregation (Ding et al. 2012). The specific interactions between the AgNP surface charges and ubiquitin residues as well as other non-specific inter-molecule interactions were modeled by atomistic DMD simulations (Ding et al. 2013).

We investigated AgNP-ubiquitin corona formation by performing DMD simulations of the coarse-grained system, with multiple ubiquitins initially positioned randomly with respect to a citrate-coated AgNP. The AgNP-ubiquitin complex structure derived from simulations had multiple ubiquitins bound to the surface of the AgNP (Figure 15.14). Depending on stoichiometry, the proteins could form either a single-layer (Figure 15.14) or a multi-layer (Figure 15.14b) protein corona around the nanoparticle. We first performed

DMD simulations of an AgNP surrounded by 25 ubiquitin molecules. In the DMD simulations, the majority of the AgNP-bound proteins stayed folded under the simulation conditions and bound to the surface of the AgNP with their helices facing the nanoparticle. In one of the simulations, one out of the 22 AgNP-bound proteins partially unfolded and the conformation was stabilized by extensive contacts with the hydrophobic surface of the AgNP (Figure 15.14a). In addition, we explored the effect of protein concentration on corona formation by performing DMD simulation for a higher ubiquitin/AgNP ratio of 50:1. In these simulations, ubiquitins competed with citrates for binding to the AgNP (Figures 15.14b and 15.14c). The final structure featured multiple layers of protein corona, whereas the
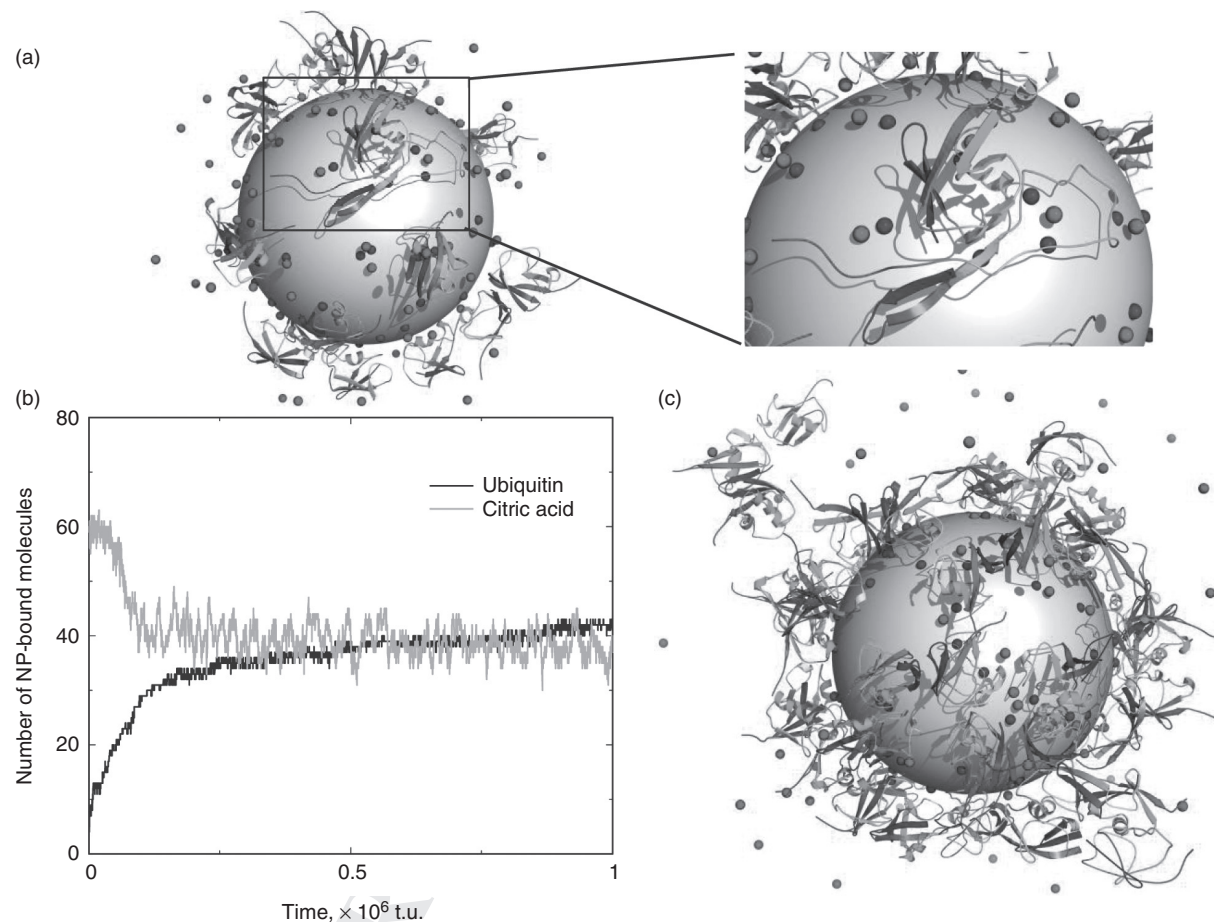
Figure 15.14. Ubiquitin-AgNP corona formation. (a) A corona structure from one of the simulations. The ubiquitins are in cartoon representation. The citrates correspond to the red spheres. The large sphere denotes the AgNP, and the small spheres on the surface of the AgNP are the positively charged atoms. One of AgNP-bound ubiquitins is unfolded on the nanoparticle surface (Right). (b) In a coarse-grained DMD simulation with a higher stoichiometric ratio of ubiquitin to AgNP (50:1), ubiquitin (lower line) competed with citrate (upper line) to bind to AgNP by displacing initially bound citrates. (e) At this high stoichiometry, multi-layers of ubiquitins were found to deposit onto the surface of the AgNP. *Source:* Ding et al. 2013. Reproduced with permission of Royal Society of Chemistry.

AU: In the caption of Figure 15.14, please avoid mentioning the color in "red spheres."

first layer was dominated by specific binding between ubiquitins and the AgNP, and the outer layers were stabilized by protein-protein interactions (Figures 15.14b and 15.14c). The AgNP-ubiquitin structures derived from the coarse-grained simulations successfully revealed an atomic picture of the nanoparticle-protein corona.

The ability of nanoparticles to induce protein unfolding (Figure 15.14a) could be one of the mechanisms of nanotoxicity. To evaluate the impact of AgNP-binding on ubiquitin conformation, we computed for each protein residue the fraction of native contacts (Q-value) (Onuchic et al. 1995) for both the AgNP-bound and unbound ubiquitins (Figure 15.15a). A residue with its Q-value close to 1 maintains a native-like structure, while losing its structure if the Q-value is near 0. Both the AgNP-bound and unbound ubiquitins maintained native-like structures with most regions

having their Q-values close to 1. Only loop regions between the secondary structures (residues 18–19, 32–35, and 46–53) had relatively low Q-values. The differences in the Q-values for AgNP-bound and unbound ubiquitins suggest that residues in contact with the AgNP were stabilized upon binding. Two regions, one near the C-terminal of the protein helix and the other close to residue 46 in a loop, were significantly destabilized upon binding. The destabilization of protein helix due to AgNP-binding is consistent with our circular dichroism (CD) measurement, which revealed that the helical content was reduced by 5% for the AgNP-bound ubiquitins compared to the free ubiquitins (Figure 15.15b). The increase of β-sheet content could be due to the formation of inter-protein hydrogen bonds between partially unfolded protein regions, since the protein concentration was locally enriched on the AgNP surface.
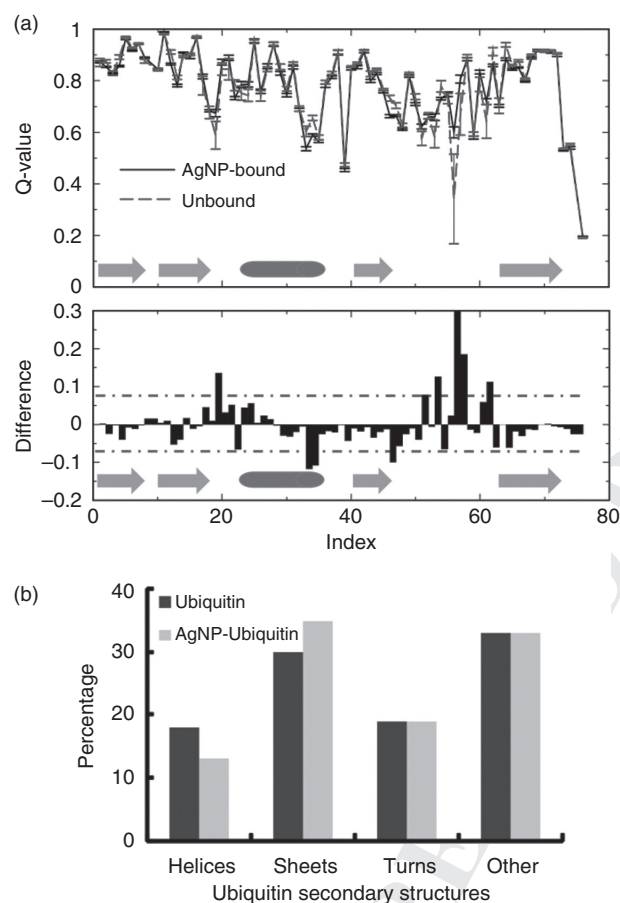
Figure 15.15. Structural changes of ubiquitin upon AgNP binding. (a) The fraction of native contacts, or Q-value, was computed for each residue for both the AgNP-bound (solid) and unbound (dashed) ubiquitins (top panel). The error bars were estimated from independent simulations. The arrows indicate the residue segments forming β-strands, and the rod denotes the residues forming the α-helix. The differences of Q-value were computed between AgNP-bound and unbound (bottom panel) cases. The two dashed lines correspond to deviations with one standard deviation above and below the average. The differences beyond the two lines are statistically significant. (b) The percentages of secondary structures in ubiquitin (darker bars) and in AgNP-ubiquitin (light bars) were probed by CD experiment. *Source:* Ding et al. 2013. Reproduced with permission of Royal Society of Chemistry.

Taken together, our new multiscale modeling has shown a remarkable predictive power for describing the structural and dynamic characteristics of nanoparticle-protein corona, a topic that is poorly understood and yet underlies our interpretation of the transformation and biocompatibility of nanoparticles in aqueous amphiphilic environments.

15.7. SUMMARY

In this chapter we have described, from a biophysical perspective, the interactions between nanoparticles and biological systems using both experimental and computational methodologies. The nanoparticles under consideration included the abundantly synthesized carbon nanotubes, fullerenes and their derivatives, graphene, graphene oxide, as well as silver nanoparticles that are used in commercial products for antibacterial purposes. We are currently expanding our scope of examination to include other major classes of nanomaterials and surface coatings, such as gold and branched polyethyleneimine (PEI)-coated AgNPs as well as dendrimers, and will report our findings at proper forums in the future. The natural amphiphiles of interest to this chapter ranged from the molecular species of gallic acid, NOM, cellulose, fatty acids, peptides, nucleic acids, tubulin, and ubiquitin that nanoparticles may encounter to render new identities of "biocoronas" to the biomolecular assemblies of lipid bilayers, mammalian and plant cells, and microtubules that nanoparticles may interact with to elicit a physical, chemical, or biological impact. Specifically, we showed the remarkable prediction power of atomistic and coarse-grained simulation approaches, which remain to be implemented as a main strategy for advancing our understanding of the environmental and biological fate of nanomaterials.

REFERENCES

Andrievsky, G. V., Klochkov, V. K., Bordyuh, A. B., and Dovbeshko, G. I. (2002). Comparative analysis of two aqueous-colloidal solutions of C_{60} fullerene with help of FTIR reflectance and UV-Vis spectroscopy. *Chem. Phys. Lett.*, **364**, 8–17.

Berendsen, H. J. C. (2007). *Simulating the Physical World: Hierarchical Modeling from Quantum Mechanics to Fluid Dynamics*. Cambridge University Press.

Brooijmans, N., and Kuntz, I. D. (2003). Molecular recognition and docking algorithms. *Annu. Rev. Biophys. Biomol. Struct.*, **32**, 335–373.

Calzolai, L., Franchini, F., Gilliland, D., and Rossi, F. (2010). Protein–nanoparticle interaction: identification of the ubiquitin–gold nanoparticle interaction site. *Nano Lett.*, **10**, 3101–3106.

Cedervall, T., Lynch, I., Lindman, S., Berggard, T., Thulin, E., Nilsson, H., Dawson, K. A., and Linse, S. (2007). Understanding the nanoparticle-protein corona using methods to quantify exchange rates and affinities of proteins for nanoparticles. *Proc. Natl. Acad. Sci. U S A*, **104**, 2050–2055.

Chen, R., Ratnikova, T. A., Stone, M., Lin, S., Lard, M., Huang, G., Hudson, J. S., and Ke, P. C. (2010). Differential uptake of carbon nanoparticles by plant and mammalian cells. *Small*, **6**, 612–617.

Cornell, W. D., Cieplak, P., Bayly, C. I., Gould, I. R., Merz, K. M. Jr., Ferguson, D. M., Spellmeyer, D. C., Fox, T., Caldwell, J. W., and Kollman, P. A. (1995). A second generation force field for the simulation of proteins, nucleic acids, and organic molecules. *J. Am. Chem. Soc.*, **117**, 5179–5197.

Ding, F., Dokholyan, N. V., Buldyrev, S. V., Stanley, H. E., and Shakhnovich, E. I. (2002a). Molecular dynamics simulation of the SH3 domain aggregation suggests a generic amyloidogenesis mechanism. *J. Mol. Biol.*, **324**, 851–858.

Ding, F., Dokholyan, N. V., Buldyrev, S. V., Stanley, H. E., and Shakhnovich, E. I. (2002b). Direct molecular dynamics observation of protein folding transition state ensemble. *Biophys. J.*, **83**, 3525–3532.

Ding, F., and Dokholyan, N. V. (2005). Simple but predictive protein models. *Trends. Biotechnol.*, **23**, 450–455.

Ding, F., Guo, W., Dokholyan, N. V., Shakhnovich, E. I., and Shea, J. E. (2005). Reconstruction of the src-SH3 protein domain transition state ensemble using multiscale molecular dynamics simulations. *J. Mol. Biol.*, **350**, 1035–1050.

Ding, F., and Dokholyan, N. V. (2006). Emergence of protein fold families through rational design. *PLoS Comput. Biol.*, **2**, e85.

Ding, F., Furukawa, Y., Nukina, N., and Dokholyan, N. V. (2012). Local unfolding of CU, ZN superoxide dismutase monomer determines the morphology of fibrillar aggregates. *J. Mol. Biol.*, **421**, 548–560.

Ding, F., and Dokholyan, N. V. (2012). Discrete molecular dynamics simulation of biomolecules. In: *Computational Modeling of Biological Systems: From Molecules to Pathways*, 55–73, edited by N. V. E. Dokholyan. Springer.

Ding, F., Radic, S., Choudhary, P., Chen, R., Brown, J. M., and Ke, P. C. (2013). Direct observation of a silver nanoparticle-ubiquitin corona formation. *Nanoscale*, **5**, 9162–9169.

Duan, Y., Wu, C., Chowdhury, S., Lee, M. C., Xiong, G., Zhang, W., Yang, R., Cieplak, P., Luo, R., Lee, T., Caldwell, J., Wang, J., and Kollman, P. (2003). A point-charge force field for molecular mechanics simulations of proteins based on condensed-phase quantum mechanical calculations. *J. Comput. Chem.*, **24**, 1999–2012.

Ge, C., Du, J., Zhao, L., Wang, L., Liu, Y., Li, D., Yang, Y., Zhou, R., Zhao, Y., Chai, Z., and Chen, C. (2011). Binding of blood proteins to carbon nanotubes reduces cytotoxicity. *Proc. Natl. Acad. Sci. U S A*, **108**, 16968–16973.

Girifalco, L. A. (1992). Molecular properties of fullerene in the gas and solid phases. *J. Phys. Chem.*, **96**, 858–861.

Gotovac, S., Honda, H., Hattori, Y., Takahashi, K., Kanoh, H., and Kaneko, K. (2007). Effect of nanoscale curvature of single-walled carbon nanotubes on adsorption of polycyclic aromatic hydrocarbons. *Nano Lett*., **7**, 583–587.

Gottschalk, F., Sonderer, T., Scholz, R. W., and Nowack, B. (2009). Modeled environmental concentrations of engineered nanomaterials (TiO$_2$, ZnO, Ag, CNT, fullerenes) for different regions. *Environ. Sci. Technol.*, **43**, 9216–9222.

Haas, A. F., and Wild, C. (2010). Composition analysis of organic matter released by cosmopolitan coral reef-associated green algae. *Aquat. Biol.*, **10**, 131–138.

Huey, R., Morris, G. M., Olson, A. J., and Goodsell, D. S. (2007). A semiempirical free energy force field with charge-based desolvation. *J. Comput. Chem.*, **28**, 1145–1152.

Humphrey, W., Dalke, A., and Schulten, K. (1996). VMD: visual molecular dynamics. *J. Mol. Graph.*, **14**, 33–38.

Hyung, H., Fortner, J. D., Hughes, J. B., and Kim, J. H. (2007). Natural organic matter stabilizes carbon nanotubes in the aqueous phase. *Environ. Sci. Technol.*, **41**, 179–184.

Jorgensen, W. L., and Tirado-Rives, J. (1988). The OPLS potential functions for proteins. Energy minimizations for crystals of cyclic peptides and crambin. *J. Am. Chem. Soc.*, **110**, 1657–1666.

Jorgensen, W. L., Maxwell, D. S., and Rives, J. T. (1996). Development and testing of the OPLS all-atom force field on conformational energetics and properties of organic liquids. *J. Am. Chem. Soc*., **118**, 11225–11236.

Katoch, J., Kim, S. N., Kuang, Z., Farmer, B. L., Naik, R. R., Tatulian, S. A., and Ishigami, M. (2012). Structure of a peptide adsorbed on graphene and graphite. *Nano. Lett.*, **12**, 2342–2346.

Ke, P. C., and Lamm, M. H. (2011). A biophysical perspective of understanding nanoparticles at large. *Phys. Chem. Chem. Phys.*, **13**, 7273–7283.

Ke, P. C., and Qiao, R. (2007). Carbon nanomaterials in biological systems. *J. Phys. Condens. Matter*, **19**, 373101-1-25.

Kim, Y., Eom, S. H., Wang, J., Lee, D.-S., Suh, S. W., and Steitz, T. A. (1995). Crystal structure of *Thermus aquaticus* DNA polymerase. *Nature*, **376**, 612–616.

Kitchen, D. B., Decornez, H., Furr, J. R., and Bajorath, J. (2004). Docking and scoring in virtual screening for drug discovery: methods and applications. *Nat. Rev. Drug Discov.*, **3**, 935–949.

Lazaridis, T., and Karplus, M. (1999). Effective energy function for proteins in solution. *Proteins*, **35**, 133–152.

Li, Y., Korolev, S., and Waksman, G. (1998). Crystal structures of open and closed forms of binary and ternary complexes of the large fragment of *Thermus aquaticus* DNA polymerase I: structural basis for nucleotide incorporation. *EMBO J.*, **17**, 7514–7525.

Lin, S., Reppert, J., Hu, Q., Hudson, J. S., Reid, M. S., Ratnikova, T. A., Rao, A. M., Luo, H., and Ke, P. C. (2009). Uptake, translocation and transmission of carbon nanomaterials in rice plants. *Small*, **5**, 1128–1132.

Lowe, J., Li, H., Downing, K., and Nogales, E. (2001). Refined structure of alpha beta-tubulin at 3.5 A resolution. *J. Mol. Biol.*, **313**, 1045–1057.

Lowry, G. V., Gregory, K. B., Apte, S. C., and Lead, J. R. (2012). Transformations of nanomaterials in the environment. *Environ. Sci. Technol.*, **46**, 6893–6899.

Lynch, I., and Dawson, K. A. (2011). Protein-nanoparticle interactions. *Nano Today*, **3**, 40–47.

Määttä, J., Lin, S., Ke, P. C., and Salonen, E. *unpublished*.

Mackerell, A. D., Feig, M., and Brooks, C. L. (2004). Extending the treatment of backbone energetics in protein force fields:

limitations of gas-phase quantum mechanics in reproducing protein conformational distributions in molecular dynamics simulations. *J. Comput. Chem.*, **25**, 1400–1415.

MacKerell A. D., Jr., Bashford, D., Bellott, M., Dunbrack, R. L., Jr., Evanseck, J., Field, M. J., Fischer, S., Gao, J., Guo, H., Ha, S., Joseph, D., Kuchnir, L., Kuczera, K., Lau, F. T. K., Mattos, C., Michnick, S., Ngo, T., Nguyen, D. T., Prodhom, B., Reiher, W. E., III, Roux, B., Schlenkrich, M., Smith, J., Stote, R., Straub, J., Watanabe, M., Wiorkiewicz-Kuczera, J., Yin, D., and Karplus, M. (1998). All-atom empirical potential for molecular modeling and dynamics studies of proteins. *J. Phys. Chem. B*, **102**, 3586–3616.

Matthes, D., and de Groot, B. L. (2009). Secondary structure propensities in peptide folding simulations: A systematic comparison of molecular mechanics interaction schemes. *Biophys. J.*, **97**, 599–608.

Maynard, A. D., Aitken, R. J., Butz, T., Colvin, V., Donaldson, K., Oberdörster, G., Philbert, M. A., Ryan, J., Seaton, A., Stone, V., Tinkle, S. S., Tran, L., Walker, N. J., and Warheit, D. B. (2006). Safe handling of nanotechnology. *Nature*, **444**, 267–269.

Meng, X., Li, B., Chen, Z., Yao, L., Zhao, D., Yang, X., He, M., and Yu, Q. (2007). Inhibition of a thermophilic deoxyribonucleic acid polymerase by fullerene derivatives. *J. Enzyme Inhib. Med. Chem.*, **22**, 293–296.

Monticelli, L. (2012). On atomistic and coarse-grained models for C_{60} fullerene. *J. Chem. Theory Comput.*, **8**, 1370–1378.

Monticelli, L., and Salonen, E. (2012). *Biomolecular Simulations – Methods and Protocols*. Humana Press.

Morris, G. M., Huey, R., Lindstrom, W., Sanner, M. F., Belew, R. K., Goodsell, D. S., and Olson, A. J. (2009). AutoDock4 and AutoDockTools4: Automated docking with selective receptor flexibility. *J. Comput. Chem.*, **30**, 2785–2791.

Nedumpully, G. P., Monticelli, L., and Salonen, E. (2012). Mechanism of taq DNA polymerase inhibition by fullerene derivatives: insight from computer simulations. *J. Phys. Chem. B*, **116**, 10676–10683.

Nel, A. E., Madler, L., Velegol, D., Xia, T., Hoek, E. M., Somasundaran, P., Klaessig, F., Castranova, V., and Thompson, M. (2009). Understanding biophysicochemical interactions at the nano-bio interface. *Nature Mater.*, **8**, 543–557.

Onuchic, J. N., Wolynes, P. G., Luthey-Schulten, Z., and Socci, N. D. (1995). Toward an outline of the topography of a realistic protein-folding funnel. *Proc. Natl. Acad. Sci. U S A*, **92**, 3626–3630.

Oostenbrink, C., Villa, A., Mark, A. E., and Van Gunsteren, W. F. (2004). A biomolecular force field based on the free enthalpy of hydration and solvation: The GROMOS force-field parameter sets 53A5 and 53A6. *J. Comput. Chem.*, **25**, 1656–1676.

Pandey, R. B., Kuang, Z. F., Farmer, B. L., Kim, S. S., and Naik, R. R. (2012). Stability of peptide (P1 and P2) binding to a graphene sheet via an all-atom to all-residue coarse-grained approach. *Soft Matter*, **8**, 9101–9109.

Qiao, R., Roberts, A. P., Mount, A. S., Klaine, S. J., and Ke, P. C. (2007). Translocation of C_{60} and its derivatives across a lipid bilayer. *Nano Lett.*, **7**, 614–619.

Radic, S., Geitner, N. K., Podila, R., Kakinen, A., Chen, P., Ke, P. C., and Ding, F. (2013). Competitive binding of natural amphiphiles with graphene derivatives. *Scientific Reports*, **3**, 2273.

Rapapport, D. C. (1997). *The Art of Molecular Dynamics Simulation*. Cambridge: Cambridge University Press.

Ratnikova, T. A., Govindan, P. N., Salonen, E., and Ke, P. C. (2011). *In vitro* polymerization of microtubules with a fullerene derivative. *ACS Nano*, **5**, 6306–6314.

Salonen, E., Lin, S., Reid, M. L., Allegood, M. S., Wang, X., Rao, A. M., Vattulainen, I., and Ke, P. C. (2008). Real-time translocation of fullerene reveals cell contraction. *Small*, **4**, 1986–1992.

Sayes, C. M., Fortner, J. D., Guo, W., Lyon, D., Boyd, A. M., Ausman, K. D., Tao, Y. J., Sitharaman, B., Wilson, L. J., Hughes, J. B., West, J. L., and Colvin, V. L. (2004). The differential cytotoxicity of water-soluble fullerenes. *Nano Lett.*, **4**, 1881–1887.

Schlick, T. (2002). *Molecular Modeling and Simulation: An Interdisciplinary Guide*. Springer.

Sein, L. T., Jr., Varnum, J. M., and Jansen, S. (1999). Conformational modeling of a new building block of humic acid: Approaches to the lowest energy conformer. *Environ. Sci. Technol.*, **33**, 546–555.

Shang, J., Ratnikova, T. A., Anttalainen, S., Salonen, E., Ke, P. C., and Knap, H. T. (2009). Experimental and simulation studies of real-time polymerase chain reaction in the presence of a fullerene derivative. *Nanotechnology*, **20**, 415101.

Sotiriou, G. A., and Pratsinis, S. E. (2010). Antibacterial activity of nanosilver ions and particles. *Environ. Sci. Technol.* **44**, 5649–54.

Sun, X., Liu, Z., Welsher, K., Robinson, J. T., Goodwin, A., Zaric, S., and Dai, H. (2008). Nano-graphene oxide for cellular imaging and drug delivery. *Nano Res.*, **1**, 203–212.

Tournus, F., Latil, S., Heggie, M. I., and Charlier, J. C. (2005). π-Stacking interaction between carbon nanotubes and organic molecules. *Phys. Rev. B*, **72**, 075431–075435.

Vroman, L. (1962). Effect of absorbed proteins on the wettability of hydrophilic and hydrophobic solids. *Nature*, **196**, 476–477.

Wiesner, M., Lowry, G. V., Alvarez, P., Dionysiou, D., and Biswas, P. (2006). Assessing the risks of manufactured nanomaterials. *Environ. Sci. Technol.*, **40**, 4336–4345.

Wong-ekkabut, J., Baoukina, S., Triampo, W., Tang, I. M., Tieleman, D. P., and Monticelli, L. (2008). Computer simulation study of fullerene translocation through lipid membranes. *Nature Nanotech.*, **3**, 363–368.

Yang, K., and Xing, B. (2007). Desorption of polycyclic aromatic hydrocarbons from carbon nanomaterials in water. *Environ. Pollut.*, **145**, 529–537.

Yang, S., Cho, S. S., Levy, Y., Cheung, M. S., Levine, H., Wolynes, P. G., and Onuchic, J. N. (2004). Domain swapping is a consequence of minimal frustration. *Proc. Natl. Acad. Sci. U S A*, **101**, 13786–13791.

Zuo, G., Huang, Q., Wei, G., Zhou, R., and Fang, H. (2010). Plugging into proteins: poisoning protein function by a hydrophobic nanoparticle. *ACS Nano.*, **4**, 7508–7514.